Distributed neural dynamics underlie the shift from movement preparation to execution

Ziwei Yin ^{1,2*}, **Jian K. Liu** ^{1,2}, **Katja Kornysheva** ^{1,3*}

[1]Center for Human Brain Health, University of Birmingham, Birmingham, UK
[2]School of Computer Science, University of Birmingham, Birmingham, UK
[3]School of Psychology, University of Birmingham, Birmingham, UK
*Correspondence: zxy370@student.bham.ac.uk, k.kornysheva@bham.ac.uk

Dissociating the neural mechanisms of movement preparation from those of execution across the brain is fundamental to understanding motor control. Invasive recordings in primary motor cortex (M1) indicate that shared neural populations support both phases by unfolding within orthogonal subspaces or "manifolds", yet whether and how these dynamics evolve across the broader set of brain regions involved in memory-guided skilled action remains poorly understood. Here, we used magnetoencephalography (MEG) data obtained during a memory-guided delayed finger-sequence task to track fast population dynamics across M1, premotor cortices, and the hippocampus. Linear discriminant analysis decoding of sequence-specific preparatory and execution patterns revealed a transition from preparation to execution patterns across all regions prior to movement onset. Importantly, the onset of execution exhibited region-specific timing, with M1 shifting last, ∼100 ms before the first button press, consistent with the established cortical motor hierarchy. Low-dimensional trajectories showed that preparatory and execution states occupied distinct manifolds, yet were not fully orthogonal, suggesting partial overlap in tuning. MEG dynamics were dominated by peri-movement phase activity in the primary motor and premotor regions. Nevertheless, above-chance sequence decoding was recoverable from all motor and premotor regions during execution and in M1 during preparation. The state shift and the decoding accuracy were driven by distributed modulations across multiple frequency bands, indicating that full-band population dynamics carry richer information than band-limited features alone. These results demonstrate that non-invasive MEG can resolve continuous, hierarchical neural state transitions in the human brain in the context of memory-guided movement control. They offer mechanistic insight into distributed motor-related brain dynamics and support developing brain-computer-interfaces that incorporate signals from multiple brain regions beyond the primary motor cortex.

Keywords: motor control, preparation, manifolds, neural dynamics, MEG, source reconstruction

1. Introduction

Coordinating skilled actions requires the nervous system to prepare upcoming movements while preventing their premature release [1]. In non-human primates, invasive recordings in the primary motor (M1) and adjacent areas have shown that preparation and execution are implemented through distinct population-level neural states that unfold within separate low-dimensional subspaces of the same motor population [2–4]. Preparatory activity evolves in an "output-null" space, enabling the retrieval of motor plans without immediate motor output, while execution occupies an "output-potent" space defined by characteristic rotational dynamics [2, 3, 5, 6]. These findings support a dynamical-systems view in which actions emerge from evolving population trajectories, i.e., dynamic response patterns rather than static tuning of individual neurones to upcoming movement features activated below or above a threshold [7].

In humans, neuroimaging can reveal large scale activity pattern transitions from preparation to execution across the brain. Here, fMRI results suggest that the control of sequence features undergoes a state shift from high-level feature separation during planning to their integration during execution across a network of motor-related cortical and subcortical areas [8, 9]. However, the temporal dynamics and geometry of this transition remain unknown. MEG/EEG provide non-invasive access to brain dynamics, including well-established oscillatory markers of movement preparation, such as beta and alpha (mu)-band desynchronisation before and during movement linked to cortical excitability, followed by their post-movement rebound linked to inhibition [10–13] and theta-band activity associated with cognitive control and memory-dependent planning [14, 15]. However, these oscillatory dynamics alone do not reveal whether preparation and execution patterns occupy distinct neural manifolds, nor how the transition between them unfolds across distributed brain regions.

Skilled actions typically require the integration of hierarchical information spanning movements sequence structure, chunk organisation and individual movements [15, 16]. Prior work shows that these levels are not represented uniformly across the motor system: M1 primarily encodes upcoming single movements [17–19], whereas lateral and medial premotor regions contain sequence-selective activity [8, 20, 21]. Further, there is growing evidence of the hippocampus supporting retrieval and control of sequential order [9, 22, 23], with hippocampal–cortical replay predicting short-term performance gains [24]. Together, this distributed architecture suggests that sequence preparation from memory recruits both motor and cognitive brain areas.

Invasive studies have largely focused on M1 and PMd, leaving it unclear how these and other motor sequence-relevant regions coordinate the transition from preparation to execution. Whether the preparatory–execution manifolds observed in M1 extend across cortical and hippocampal networks, and how their dynamics unfold in time, remains unknown.

Here, we examined source-resolved MEG obtained during a memory-guided finger-sequence task to probe the preparatory–execution state transition non-invasively and access its organisation across motor, premotor and hippocampal regions. We further asked whether oscillatory MEG dynamics track the transition and support the decoding of upcoming sequence identity. Our results reveal a global shift across distinct manifolds toward execution-related patterns prior to movement onset, with evidence of hierarchical timing across premotor and primary motor regions, and sequence-specific information detectable in primary motor areas even before movement execution. These results demonstrate that non-invasive MEG can resolve continuous, hierarchical state transitions and reveal distributed population dynamics underlying sequential action in the human brain.

2. Results

2.1. Oscillatory markers of motor excitation, inhibition and serial recall converge in M1

To dissociate the preparatory and executive patterns that support memory-guided sequential movements across motor and hippocampal circuits, we analysed the MEG dataset from Kornysheva et al. [25]. In a delayed finger sequence task, participants learned to retrieve a five-element finger sequence and its associated target timing from memory cued by an abstract visual stimulus (Sequence Cue), and then to execute the sequence on a response keyboard following a Go Cue (Fig. 1a). We applied linearly constrained minimum variance (LCMV) beamforming to localise neural activity from regions of interest reported in our recent fMRI studies involving a similar paradigm [8, 9] - the contralateral primary motor cortex (M1), dorsal premotor cortex (PMd), supplementary motor area (SMA), ventral premotor cortex (PMv), pre-supplementary motor area (pre-SMA), and the hippocampus (Fig. 1c).

As expected, we observed neurophysiological markers of movement-related neural excitation and inhibition [13] - beta and alpha (mu) band event-related desynchronisation (ERD) during sequence preparation and execution, and a post-movement beta rebound (PMBR, Fig. 1c). Here, M1 was the only region with significant ERD during the preparation phase. ERD in M1 started on average 1.6 seconds prior to the Go Cue and lasted until the end of execution -1.6 – 3.8 s, 9 – 46 Hz, $p < .001$. This effect followed smaller ERD clusters in premotor areas: PMd (0.2 – 3.1 s, 9 – 47.5 Hz, $p < .001$), PMv (0.2 – 3.85 s, 9 – 35 Hz, $p < .001$), SMA (0.2 – 4.15 s, 8.5 – 44.5 Hz, $p < .001$), and pre-SMA (0.15 – 1.05 s, 18.5 – 37.5 Hz, $p = .001$; 1.15 – 3.1 s, 9.5 – 37 Hz, $p < .001$).

PMBR showed the most pronounced modulation in contralateral M1 (4.9 – 5.85 s, 14 – 46.5 Hz, $p = .006$) and PMd (4.85 – 6.5 s, 12.5 – 48.5 Hz, $p = .003$), followed by PMv (4.9 – 5.85 s, 18 – 39.5 Hz, $p = .012$), SMA (5.3 – 5.5 s, 19 – 44 Hz, $p = .019$), and pre-SMA (5.3 – 5.6 s, 15.5 – 43.5 Hz, $p = .014$). Several beta desynchronisation clusters distributed across the execution period were also found in the hippocampus (0.15 – 1.15 s, 17.5 – 51 Hz, $p < .001$; 1.35 – 3.65 s, 13 – 39.5 Hz, $p < .001$; 4.1 – 4.2 s, 17 – 21.5 Hz, $p = .035$, 5.35 – 6.7 s, 7.5 – 19.5 Hz, $p = .002$), but no PMBR. Instead, the hippocampus showed a high-gamma cluster after movement termination (5.2 – 5.25 s, 59.5 – 80 Hz, $p = .01$).

Increases in theta- and delta-band power were observed across all regions during both preparation and execution, in line with their role in memory and serial recall and their expected distribution across both hippocampal and cortical sources [26, 27]. Clusters were found in M1 (-1.9 – -1.3 s, 2 – 5 Hz, $p = .043$; 0.1 – 5.7 s, 2.5 – 5 Hz, $p = .015$); PMd (-1.85 – -1.1 s, 2 – 4.5 Hz, $p = .035$; 0.15 – 3.45 s, 2.5 – 5.5 Hz, $p = .013$); PMv (-2 – -0.95 s, 2 – 5.5 Hz, $p = .02$; 0.05 – 3.45 s, 2.5 – 5.5 Hz, $p = .01$); SMA (-1.95 – -1.1 s, 2.5 – 6 Hz, $p = .018$; 0.1 – 4.15 s, 2.5 – 5.5 Hz, $p = .006$); pre-SMA (-1.9 – -1.0 s, 1.5 – 5.5 Hz, $p = .011$; -0.1 – 4.05 s, 2 – 6.5 Hz, $p < .001$); and the the hippocampus (-2 – -0.55 s, 2 – 6.5 Hz, $p = .004$; -0.05 – 2.55 s, 3 – 6 Hz, $p = .002$; 3.05 – 3.5 s, 3 – 6.5 Hz, $p = .029$).

These time-frequency results confirm the predicted oscillatory markers in motor, premotor and hippocampal regions during a memory-guided motor sequence sequence tasks. Further, they indicate that contralateral M1, the principal cortical output area, is pre-activated during sequence preparation and shows all task-related band modulations observed in upstream areas.

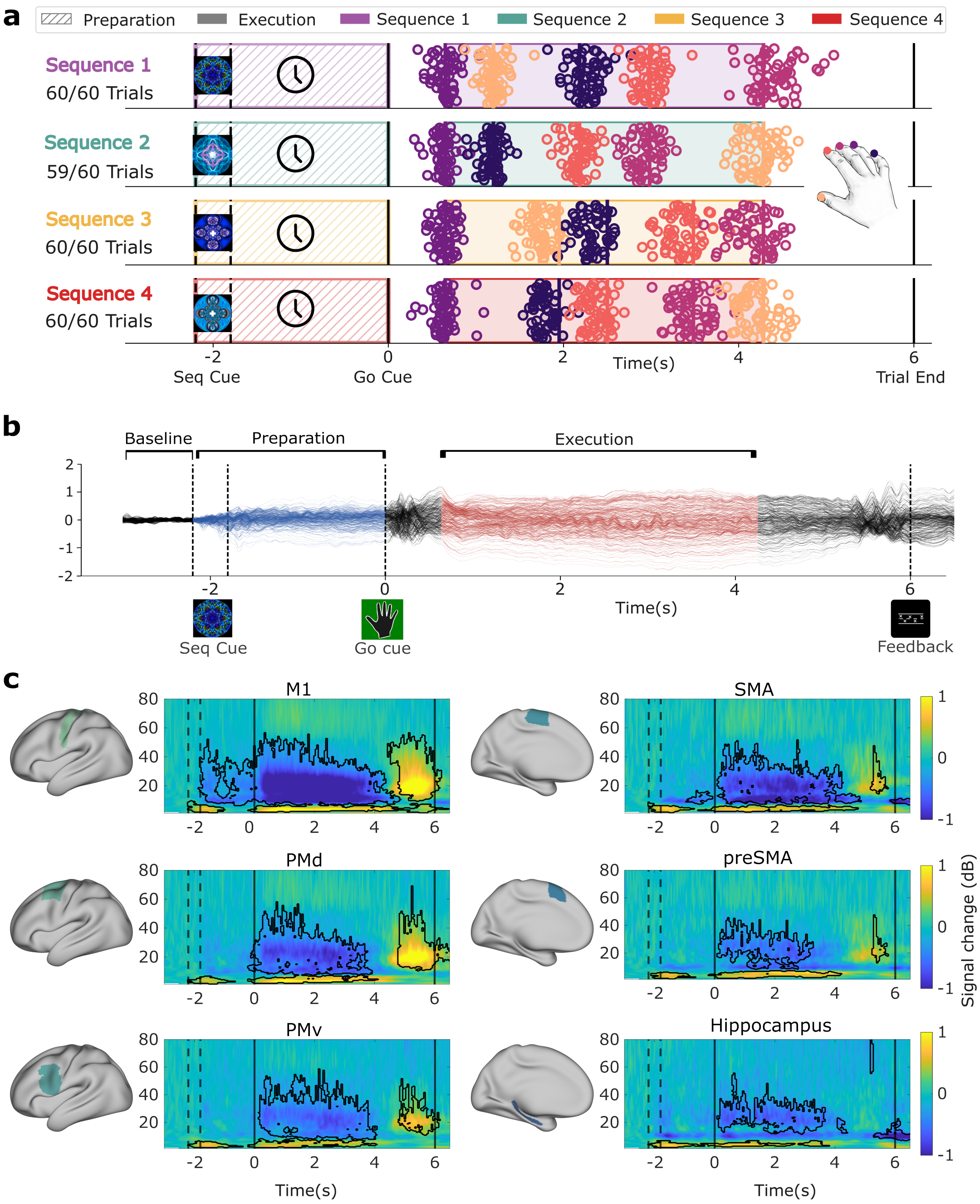
a
Preparation
Execution
Sequence 1
Sequence 2
Sequence 3
Sequence 4
Sequence 1
60/60 Trials
Sequence 2
59/60 Trials
Sequence 3
60/60 Trials
Sequence 4
60/60 Trials
-2
Seq Cue
0
Go Cue
2
Time(s)
4
6
Trial End
b
Baseline
Preparation
Execution
2
1
0
-1
-2
-2
0
2
4
6
Time(s)
Seq Cue
Go cue
Feedback
c
M1
SMA
PMd
preSMA
PMv
Hippocampus
80
60
40
20
-2
0
2
4
6
Time(s)
1
0
-1
Signal change (dB)

Figure 1: **Delayed finger sequence task and time frequency representations**
(a) Task design and representative behavioural data from a single participant. Participants memorised four five-finger tapping sequences over two days before the MEG sessions. The sequences formed a factorial combination of two temporal interval patterns and two finger orderings. During the recording session, each sequence was performed 60 times, with incorrect trials excluded from analysis. The data is aligned to the Go Cue; two black dash vertical line mark the variable delay period (1.8, 2.0, or 2.2 s) between the Sequence Cue and the Go Cue. Raster dots represent individual finger presses on each trial, colour-coded by finger identity. The coloured vertical bars indicate the planned timing of each finger press in the memorised sequence. Only trials classified as correct were shown and included in subsequent analyses. **(b)** Overview of task structure and MEG channel activity averaged across trials and participants. The blue colour indicates the preparation phase spanning the Sequence Cue and the Go Cue; the red colour indicates the execution phase between the first finger press and the last press. **(c)** Time-frequency representations (TFRs) showing source-localised oscillatory dynamics from six regions of interest: M1, PMd, SMA, pre-SMA, PMv and hippocampus. Each panel is paired with the anatomical mask used for source reconstruction. Individual TFRs were baseline-corrected using decibel (dB) normalisation relative to each participant's own baseline period, then group-averaged and baseline demeaned. Black contours indicate significant time–frequency clusters relative to baseline.

2.2. Timing of the transition from preparation to execution patterns

To uncover the timing of the neural transition between sequence preparation and execution states, we trained and tested a linear discriminant analysis (LDA) classifier with eight classes on trial-by-trial MEG patterns, including each of the four sequences during preparation and execution, respectively, from each of the six regions. For LDA training, we defined the preparatory phase as the period between the Sequence cue and the Go Cue. The execution phase was defined as the period between the first and the last press (Fig. 2a). If sequence tuning generalised across phases, classifier accuracy of sequence execution-specific patterns would have matched those during preparation, and vice versa. Alternatively, the two representations would be specific to their LDA training phase only.

The resulting sequence probability time courses showed distinct and temporally non-overlapping sequence patterns (Fig.2 b-c): execution related sequence classification accuracy remained below chance during the preparatory period, including shortly after the Go Cue, and rose significantly above chance only shortly before execution. Preparatory tuning showed the opposite pattern, with a brief gap in between phases where neither phase reached significance. This stark result confirmed that the preparation and execution phases are associated with distinct neural sequence tuning patterns that do not generalise across phases.

To resolve the timing of the offset of the preparatory sequence patterns and the onset of the execution patterns above chance, the classifier probabilities were aligned to two behavioural anchors: the Go Cue and the first movement (button press). Significance testing against temporally permuted predictions showed that neural transitions consistently occurred after the Go Cue and before movement initiation (Fig.2 b-c). The offset of sequence preparation patterns was quantified for each region: M1: 0.52 ± 0.19 s; PMd: 0.41 ± 0.31 s; PMv: 0.44 ± 0.23 s; SMA: 0.41 ± 0.33 s; pre-SMA: 0.32 ± 0.33 s; hippocampus: 0.22 ± 1.05 s (Fig.2d, upper panel). Pairwise Wilcoxon rank-sum tests confirmed a significant difference between M1 and pre-SMA, $p = .001$. Similarly, the onset of the sequence execution patterns differed across regions: M1: -0.14 ± 0.13 s; PMd: -0.23 ± 0.23 s; PMv: -0.16 ± 0.17 s; SMA: -0.39 ± 0.43 s; pre-SMA: -0.62 ± 0.64 s; hippocampus: -0.62 ± 0.62 s (Fig.2d, lower panel). Pairwise Wilcoxon rank-sum tests confirmed a significant difference between M1 and pre-SMA ($p = .010$), and M1 versus SMA: ($p = .048$).

To investigate whether the timing of the neural patterns transitions followed the motor hierarchy, we fitted linear mixed-effects models. The hierarchical order was defined by the proximity of regions to the periphery, i.e. in line with the reported anatomical density of direct cortico-spinal projections to the lower cervical segments of the spinal cord (C7–T1) and cortico-cortical connectivity to M1, from furthest to closest: Hippocampus, pre-SMA, SMA, PMv, PMd and M1. Whilst the offset of preparation patterns showed no evidence of a hierarchical shift [28] ($\beta_0 = 0.465, \beta_1 = -0.00057, \beta_1^* = -0.002, p = .984$), the onset of execution revealed a significant positive slope, with transitions occurring progressively later along the motor hierarchy, with M1 transitioning last to execution patterns($\beta_0 = -0.607, \beta_1 = 0.077, \beta_1^* = 0.326, p < .001$).

When the execution prediction curve was correlated with spectral power in different canonical frequency bands, most significant clusters were clustered around the phase transition (Fig.2e). Significant M1 clusters observed in delta (-0.11 – 0.34 s, $p < .001$; 0.40 – 0.54 s, $p = .025$), theta (-0.23 – 0.13 s, $p = .003$; 0.45 – 0.57 s, $p = .020$), alpha (-0.24 – 0.17 s, $p = .002$; 0.27 – 0.56 s, $p = 0.002$), beta (-0.22 – 0.15 s, $p = .005$; (0.41 – 0.55 s, $p = 0.033$), gamma (-0.14 – 0.23 s, $p = .004$). PMd observed significant delta (-0.11 – 0.18 s, $p = 0.005$), theta (-0.23 – 0.19 s, $p < .001$), alpha (-0.20 – 0.15 s, $p = .002$), beta (-0.22 – 0.19 s, $p = .002$; 0.40 – 0.55 s, $p = .023$), gamma (-0.15 – 0.04 s, $p = .015$; 0.38 – 0.58 s, $p = .021$) clusters. PMv also observed significant clusters in all frequency bands, delta (-0.15 – 0.20 s, $p = .001$; 0.42 – 0.55 s, $p = .039$), theta (0.09 – 0.19 s, $p = .020$; 0.33 – 0.54 s, $p = .003$), alpha (-0.20 – 0.03 s, $p = .005$; 0.09 – 0.27 s, $p = .022$), beta (-0.18 – 0.48 s, $p = .001$), gamma(-0.20 – 0.27 s, $p = .001$). SMA observed delta (-0.10 – 0.16 s, $p = .002$; 0.34 – 0.43 s, $p = .032$), theta (-0.11 – 0.43 s, $p = .002$), alpha (-0.16 – 0.20 s, $p = .001$), beta (-0.25 – 0.17 s, $p = .002$), gamma (-0.13 – 0.29 s, $p = .002$). Pre-SMA observed delta (-0.08 – 0.25 s, $p = .001$; 0.34 – 0.57 s, $p = .003$), theta (-0.14 – 0.12 s, $p = .002$; 0.21 – 0.33 s, $p = 0.035$; 0.72 – 0.80 s, $p = .040$), alpha (-0.17 – 0.12 s, $p < .001$; 0.40 – 0.51 s, $p = 0.030$), gamma (-0.16 – 0.13 s, $p = .004$). Hippocampus only showed significant correlation in theta band (-0.24 – -0.14 s, $p = .017$; 0.08 – 0.18 s, $p = .017$).

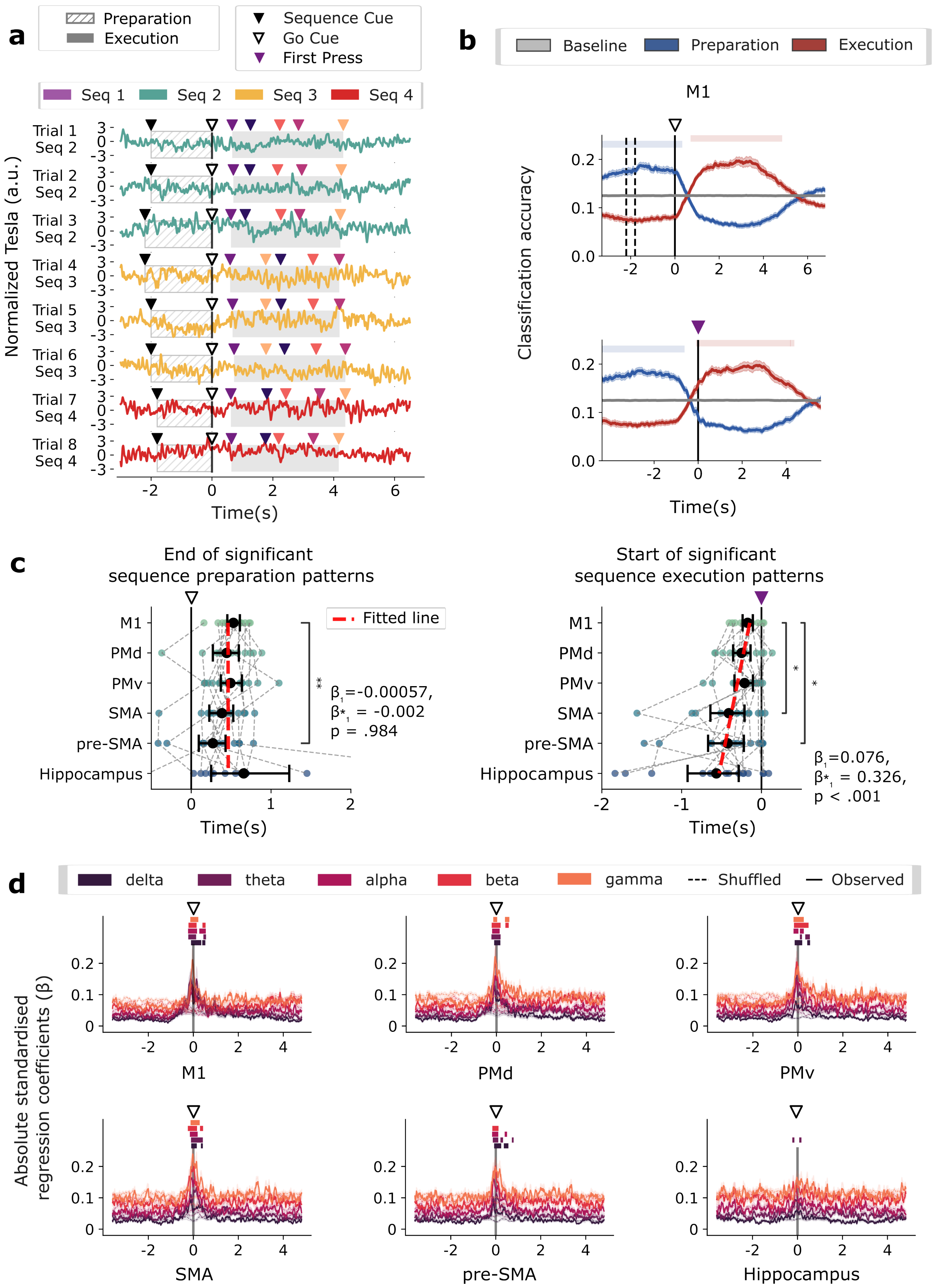
a
Preparation
Execution
Sequence Cue
Go Cue
First Press
Seq 1
Seq 2
Seq 3
Seq 4
Normalized Tesla (a.u.)
Trial 1 Seq 2
Trial 2 Seq 2
Trial 3 Seq 2
Trial 4 Seq 3
Trial 5 Seq 3
Trial 6 Seq 3
Trial 7 Seq 4
Trial 8 Seq 4
3
0
-3
-2
0
2
4
6
Time(s)
b
Baseline
Preparation
Execution
M1
Classification accuracy
0.0
0.1
0.2
Time(s)
c
End of significant sequence preparation patterns
Fitted line
M1
PMd
PMv
SMA
pre-SMA
Hippocampus
**
β₁=-0.00057,
β*₁ = -0.002
p = .984
Time(s)
Start of significant sequence execution patterns
*
*
β₁=0.076,
β*₁ = 0.326,
p < .001
-2
-1
0
1
2
d
delta
theta
alpha
beta
gamma
Shuffled
Observed
Absolute standardised regression coefficients (β)
0
0.1
0.2
M1
PMd
PMv
SMA
pre-SMA
Hippocampus

Figure 2: **LDA quantifies temporal transitions between motor preparation and execution.** **(a)** Schematic of the eight-class Linear Discriminant Analysis (LDA) training. The LDA discriminates between combinations of sequence identity and phase (e.g., Seq1 x Prep, Seq2 x Exec) and is trained on 200 Hz raw source dynamics taken from individual trials based on the variable Go Cue delay and finger presses. The plot shows example data from one channel over 12 trials. Sampling windows were aligned to trial-specific behavioural markers, with an equal number of samples drawn from each phase. To account for class imbalance, 40 trials were sampled per sequence, and results were averaged over 1,000 bootstrap repetitions. **(b)** LDA classification accuracy across participants (n = 14) for M1, aligned to the Go Cue (top) or the first button press (bottom). Curves reflect the probability assigned to the correct sequence–phase class (e.g., Seq1-Prep / Seq1-Exec for sequence-1 trials). Traces indicate participant averages, with shaded regions denoting standard error. Semi-transparent shading at the top of each plot marks significant intervals relative to the shuffled baseline (cluster forming alpha < .01, final threshold <.05). Preparatory and execution predictions exhibit temporally non-overlapping patterns. **(c)** The timing of offset of significant preparation patterns aligned to go cue (Top) and the timing of onset of significant execution patterns aligned to first press (Bottom) across motor areas and the hippocampus. Connecting lines represent data from individual participants (n = 14). Statistical comparisons were performed using Wilcoxon rank-sum tests with BH–FDR correction across 15 comparisons. Red dashed lines show the fitted linear mixed-effects models computed from subject-averaged transition timings. Corresponding model outputs are added in the text next to panels. **(d)** Rectified standardised regression coefficients relating the execution-probability time course to canonical frequency-band activity. Colours denote frequency bands. Shading at the top of each plot marks significant intervals relative to the permuted-correlation baseline (circular-shift null, averaged over 1,000 permutations). Both the execution-probability time course and the TFR-derived band-power signals were z-scored across the whole trial prior to correlation. Correlations were computed using a sliding window (200 ms window, 10 ms step).

2.3. Principal component analysis reveal distinct preparation and execution manifolds

Next, we applied principal component analysis (PCA) to embed high-dimensional source MEG dynamics into three-dimensional manifolds. This approach reveals the geometric structure underlying movement-related dynamics across multiple brain regions, enabling a more direct comparison with invasive animal recordings [2, 5]. The first three principal components captured the majority of the variance across all regions (Fig.3; M1: $90.5 \pm 3.3\%$; PMd: $94.9 \pm 1.7\%$; PMv: $93.3 \pm 2.2\%$; SMA: $97.5 \pm 1.1\%$; pre-SMA: $97.7 \pm 0.7\%$; hippocampus: $99.2 \pm 0.3\%$).

When projected into this low-dimensional space, trajectories from the preparation and execution phases occupied distinct manifolds, showing differential distributions between phases along the principal component axes (Fig.3a). This phase separation was confirmed by statistically significant Kolmogorov–Smirnov (KS) distances between the preparation and execution distributions along each PC axis, evaluated against a permutation-based null distribution and present in all regions of interest (Fig.3b; Wilcoxon signed-rank tests, false discovery rate controlled using Benjamini-Hochberg (FDR-BH) across 6 areas × 3 PCs; all $p < .001$).

Furthermore, the Euclidean distance between the phase clusters in the low-dimensional space was significantly greater than chance in all regions (Fig.3c; Wilcoxon signed-rank tests; Bonferroni corrected across 6 regions; M1: 2.31 ± 0.43, $p < .001$; PMd: 2.30 ± 0.42, $p < .001$; PMv: 2.27 ± 0.45, $p = .002$; SMA: 2.30 ± 0.48, $p = .001$; pre-SMA: 2.27 ± 0.39, $p = .001$; hippocampus: 2.36 ± 0.46, $p = .001$). The largest separations were observed in M1 and the hippocampus, with slightly smaller distances in the remaining motor regions. There were no significant differences in distances between areas (Friedman test: $\chi^2(5) = 2.12$, $p = .832$).

PCA was computed using covariance matrices averaged across the full trial. To test whether the preparatory and execution periods nevertheless exhibit distinct covariance patterns, we computed covariance matrices in a sliding-window fashion and quantified the similarity between preparatory and execution matrices. The correlation metric is unchanging with respect to scale; therefore, the distance between phases indicates that execution is not simply a weaker or scaled version of preparation. In all regions, the correlation between preparatory and execution covariance matrices was significantly lower than expected by chance (Fig.3d; Wilcoxon signed-rank tests against permutation; Bonferroni corrected across 6 regions; $p = .004$ for all regions; M1: 0.0017 ± 0.0009; PMd: 0.0011 ± 0.0017; PMv: 0.0008 ± 0.0005; SMA: 0.0016 ± 0.0023; pre-SMA: 0.0009 ± 0.0013; hippocampus: 0.0004 ± 0.0002). The Friedman test indicated a significant effect of region, $\chi^2(5) = 11.14$, $p = .049$, but no pairwise Wilcoxon signed-rank comparisons survived FDR-BH across 15 area pairs.

Previous research highlighted the geometric orthogonality between the preparatory and execution dynamics [3]. To examine this in our data, we fitted a Gaussian mixture model (GMM) to each state within the three-dimensional PCA space and compared the angles between their respective hyperplanes (Fig. 3e). The resulting angles were neither parallel ($0°$) nor orthogonal ($90°$) to each other (M1: $46.7 \pm 23.1°$; PMd: $38.4 \pm 22.8°$; PMv: $51.2 \pm 24.9°$; SMA: $45.1 \pm 19.2°$; pre-SMA: $60.6 \pm 24.0°$; hippocampus: $50.0 \pm 26.3°$; Wilcoxon signed-rank tests, Bonferroni-corrected across 6 regions; $p < .001$ for all comparisons).

Following the established subspace analysis [4], we projected the subspace defined by execution-only dynamics onto the subspace derived from preparation-only dynamics. The resulting alignment index revealed that the preparatory and execution dynamics occupy highly similar low-dimensional manifolds, as reflected by the high alignment index (Fig. 3e; M1: 0.997 ± 0.0019; PMd: 0.994 ± 0.011; PMv: 0.956 ± 0.088; SMA: 0.955 ± 0.0085; pre-SMA: 0.998 ± 0.0018; Hippocampus: 0.999 ± 0.0010). However, when tested against the perfect alignment (index = 1), all areas showed alignment indices significantly below 1 (Wilcoxon signed-rank tests, Bonferroni-corrected across 6 regions; all $p < .001$). Moreover, the group passed the Friedman test ($\chi^2(5) = 16.735$; $p = .005$) and hippocampus exhibited higher alignment than motor areas (PMv vs. hippocampus: $p = .005$; SMA vs. hippocampus: $p = .009$; Wilcoxon rank-sum tests, BH–FDR corrected across 15 comparisons).

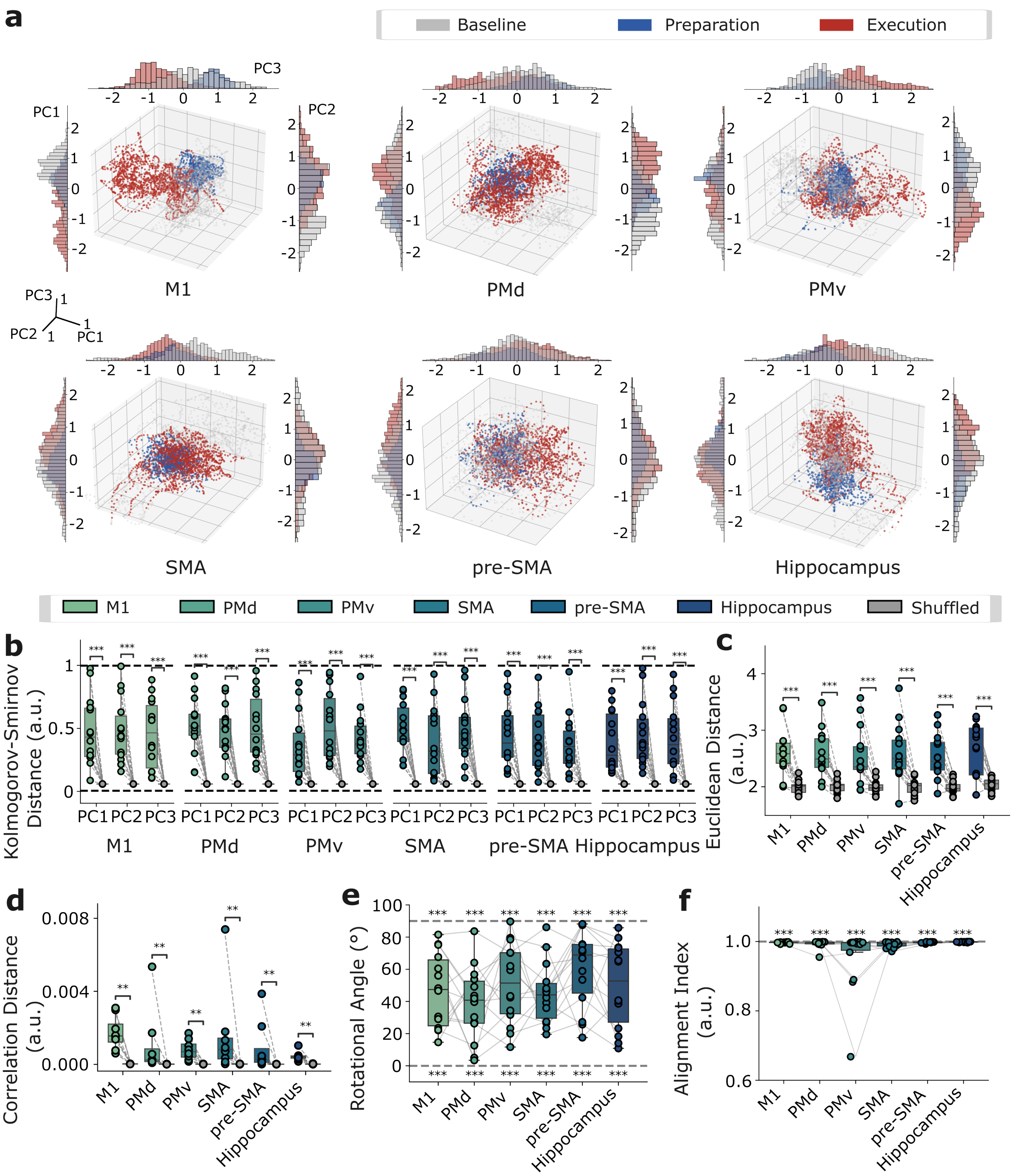
a
Baseline
Preparation
Execution
PC1
PC2
PC3
M1
PMd
PMv
SMA
pre-SMA
Hippocampus
M1
PMd
PMv
SMA
pre-SMA
Hippocampus
Shuffled
b
Kolmogorov-Smirnov Distance (a.u.)
PC1 PC2 PC3
c
Euclidean Distance (a.u.)
d
Correlation Distance (a.u.)
e
Rotational Angle (°)
f
Alignment Index (a.u.)
***
**

Figure 3: **Preparation and execution occupy distinct subspaces in shared low-dimension manifold. (a)** Source-localised MEG data projected onto the first three principal components for an example participant. All axis were z-scored. Trajectories show sequence-averaged dynamics, colour-coded by phase (preparation, execution). Marginal histograms indicate the distribution of data points along each principal component axis for each phase. **(b)** Kolmogorov–Smirnov (KS) distances between preparatory and execution dynamics along individual principal components. The KS distance (range: 0–1) quantifies the maximum difference between the empirical distributions of two samples. Each dot represents one participant (N = 14). The mean distance for each participant is generated by bootstrap in which 500 data points were drawn, and the KS distance was bootstraped across 1,000 iterations. A permutation test was performed by randomly reassigning samples between phases to generate a null distribution. **(c)** Euclidean distance between preparatory and execution trajectories in the 3D PCA space. For each participant, the mean distance from execution points to the preparatory centroid was compared to a null distribution obtained by randomly permuting phase labels (500 samples per group, 1,000 iterations). **(d)** Correlation distance between phase-average covariance matrices indicate significant phase difference (Wilcoxon signed-rank tests, Bonferroni-corrected across 6 regions; $p < .01$ for all comparisons). **(e)** Angle between the directions of maximum variance of the preparatory and execution Gaussian mixture models (GMMs). This angle reflects the difference in orientation between the two dominant axes of variation. The resulting angles were neither parallel (0°) nor orthogonal (90°) to each other (Wilcoxon signed-rank tests, Bonferroni-corrected across 6 regions; $p < .001$ for all comparisons). **(f)** Alignment index quantifying the similarity between neural manifolds formed by preparatory and execution dynamics. Values approaching 1 indicate stronger alignment, suggesting that both phases occupy similar subspaces. Wilcoxon signed-rank test against full alignment (1) is $p < .001$ for all areas (Bonferrion correction over 6 areas).

2.4. MEG covariance pattern separation is driven by phase, not sequence identity

To extract the temporal evolution of high-dimensional covariance matrices, we used a sliding window approach, which captures the internal functional connectivity or spatial coordination among local neural populations. These matrices were then embedded into a low-dimensional space by t-distributed Stochastic Neighbor Embedding (t-SNE), providing a sensitive probe of phase- and sequence-specific neural coding dynamics across brain regions during motor behaviour (Fig.4a). Critically, this analysis highlighted heterogeneity in how different brain regions traversed this phase transition: The primary motor cortex (M1) showed greatest temporal continuity reflected by the smallest consecutive distances (Fig.4b; M1: 0.848 ± 0.332; PMd: 1.839 ± 0.845; PMv: 1.756 ± 0.899; SMA: 3.145 ± 1.326; pre-SMA: 3.677 ± 1.887; Hippocampus: 4.210 ± 0.959). In contrast, the hippocampus displayed a more scattered and discontinuous trajectory, indicating weaker internal organisation or sequential changes in local coordination relative to the task phases. A Friedman test confirmed robust regional differences in trajectory continuity ($\chi^2(5) = 60.204$, $p < .001$). Post-hoc Wilcoxon rank-sum tests with BH-FDR across 15 area pairs revealed significant distances among many regions (following pairs have $p < .001$: M1 vs. PMd, M1 vs. PMv, M1 vs. SMA, M1 vs. pre-SMA, M1 vs. hippocampus, PMd vs. SMA, PMd vs. pre-SMA, PMd vs. hippocampus; PMv vs. pre-SMA, PMv vs. hippocampus; other significant pairs: PMv vs. SMA: $p = .003$; SMA vs. hippocampus: $p = .021$).

Next, we quantified the distance between low dimensional phase clusters, which provides a measure of preparatory-to-execution progression (Fig.4c; M1: 32.02 ± 2.73; PMd: 29.62 ± 3.73;PMv: 29.78 ± 3.20; SMA: 29.06 ± 3.61; pre-SMA: 28.52 ± 3.45; Hippocampus: 27.41 ± 3.16;). M1 showed significantly greater phase separation than other regions (Friedman test: $\chi^2(5) = 16.490$, $p = .006$; post-hoc Wilcoxon rank-sum tests, BH-FDR corrected over 15 comparisons: M1 vs. PMd: $p = .009$; M1 vs. SMA: $p = .025$; M1 vs. pre-SMA: $p = .009$; M1 vs. Hippocampus: $p = .009$), suggesting a structured, continuous remapping of spatial coding underlying motor control. This suggests that phase transitions are not merely governed by scaling a fixed pattern, but rely on gradual, structural shifts in spatial neural coding.

To quantify this statistically, we sought to dissociate the variance arising from time-dependent changes, sequence identity by applying demixed principal component analysis (dPCA). This method extends PCA by constraining components to separately capture variance attributable to time, sequence identity, or their interaction. The majority of variance was aligned with the temporal transition, with the hippocampus exhibiting the least variance and M1 showing the highest variance among motor regions (Fig.4d; M1: $16.37 \pm 9.37\%$; PMd: $15.72 \pm 13.64\%$;PMv: $9.70 \pm 5.55\%$; SMA: $6.77 \pm 5.00\%$; pre-SMA: $5.46 \pm 6.14\%$; Hippocampus: $1.34 \pm 1.31\%$). In contrast, components specifically attributed to sequence identity accounted for only a small proportion of the total variance and showed weaker separability across sequences (Fig.4d; time x sequence: M1: $1.65 \pm 1.04\%$; PMd: $1.29 \pm 0.59\%$;PMv: $1.55 \pm 1.00\%$; SMA: $1.26 \pm 1.41\%$; pre-SMA: $0.99 \pm 0.97\%$; Hippocampus: $0.76 \pm 1.76\%$; sequence: M1: $0.11 \pm 0.12\%$; PMd: $0.09 \pm 0.23\%$;PMv: $0.11 \pm 0.13\%$; SMA: $0.05 \pm 0.08\%$; pre-SMA: $0.07 \pm 0.07\%$; Hippocampus: $0.03 \pm 0.06\%$;). Comparing different stimulus variance within the area showed significance (Wilcoxon rank-sum tests, BH-FDR corrected over 3 x 6 comparisons; $p < .001$ for all pairs except for hippocampus time versus time x sequence: $p = .03$).

When comparing across areas, Pre-SMA and SMA showed lower explained variance by the sequence X time and sequence components than M1 (sequence X time: Friedman test: $\chi^2(5) = 27.88$, $p < .001$; Wilcoxon rank-sum test; BH-FDR corrected over 15 pairs: M1 vs. pre-SMA: $p = .040$, M1 vs. Hippocampus: $p = .040$, PMd vs. Hippocampus: $p = .042$, PMv vs. Hippocampus: $p = .040$, SMA vs. Hippocampus: $p = .040$, pre-SMA vs. Hippocampus: $p = .040$), (sequence: Friedman test: $\chi^2(5) = 19.55$, $p = .002$; Wilcoxon rank-sum test; BH-FDR corrected over 15 pairs: M1 vs. SMA: $p = .034$, M1 vs. Hippocampus: $p = .034$, PMv vs. Hippocampus: $p = .034$).

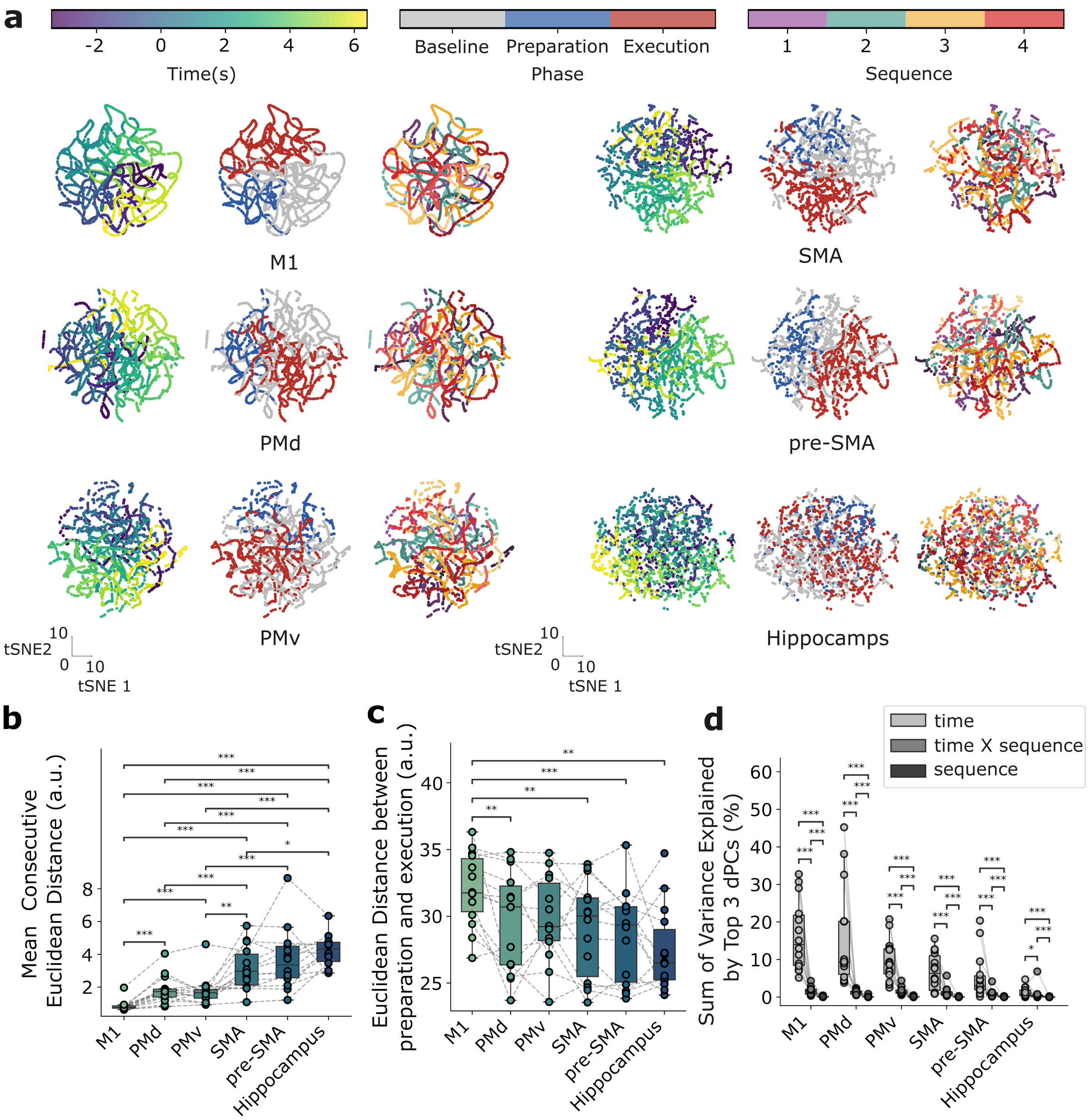
a
-2
0
2
4
6
Time(s)
Baseline
Preparation
Execution
Phase
1
2
3
4
Sequence
M1
SMA
PMd
pre-SMA
PMv
Hippocamps
tSNE2
10
0
10
tSNE 1
b
Mean Consecutive Euclidean Distance (a.u.)
2
4
6
8
M1
PMd
PMv
SMA
pre-SMA
Hippocampus
***
**
*
c
Euclidean Distance between preparation and execution (a.u.)
25
30
35
40
**
***
d
Sum of Variance Explained by Top 3 dPCs (%)
0
10
20
30
40
50
60
time
time X sequence
sequence

Figure 4: **Time-resolved covariance structure reveals phase-specific clustering**
(a) Example t-distributed Stochastic Neighbor Embedding (t-SNE) embedding of time-resolved covariance matrices six regions of interest (M1, PMd, PMv, SMA, pre-SMA, hippocampus). Covariance matrices were computed using 200Hz binned data with 200ms sliding window and 10ms stepsize and embedded into a 2D t-SNE space. Each subpanel consists of three small plots showing continuous time label (left), phase label(middle), sequence label(right). **(b)** Mean consecutive Euclidean distance between adjacent time points in the t-SNE space, averaged across participants. Smaller distances indicate smoother, more temporally continuous trajectories, whereas larger distances reflect discontinuous or irregular transitions. Horizontal brackets denote significant pairwise differences (Wilcoxon rank-sum test, BH–FDR corrected over 15 comparisons). **(c)** Euclidean distance between preparatory and execution clusters within the t-SNE embedding, quantifying phase separation in each region. M1 exhibits significantly greater separation than other regions, indicating a sharper transition between preparatory and execution states. Individual participant values are shown with paired lines. Horizontal brackets denote significant pairwise differences (Wilcoxon rank-sum test, BH–FDR corrected). **(d)** Variance explained by the top three demixed PCA (dPCA) components for each region, decomposed into contributions from time, sequence, and time × sequence factors. Each dot represents one participant; boxplots show group distributions. Asterisks mark significant differences between component types within region (Wilcoxon signed-rank tests, BH–FDR corrected). **(e)** Time-resolved Euclidean distance between preparatory and execution covariance matrices, averaged across participants. Distances were computed in a sliding window aligned to key behavioural markers (Go cue: dashed lines; first movement: solid line). Shaded regions show SEM. Phase separation increases sharply after the Go cue, consistent with state transitions revealed in the t-SNE analysis.

2.5. Decoding sequence identity

Finally, we set out to test whether sequence-specific patterns, whilst distinct across phases, could be utilised to decode the sequence identity. We applied sliding window LDA, training and testing within the same peri-movement phase, to probe when sequence identity could be recovered during preparation and production. (Fig.5a). Decoding accuracy significantly exceeded the shuffled baseline, primarily during execution in all motor regions, but not significantly in the hippocampus. M1 was the only region from which sequence identity could be reliably recovered during sequence preparation (-1.66 – 1.17 s).

To evaluate the spectral contributions to decoding, trial-wise LDA outputs were regressed onto z-scored power in canonical frequency bands (Fig. 5b). The resulting regression coefficients were temporally unstable, and most did not exceed significance relative to the shuffled correlation baseline, suggesting that no individual frequency band reliably drives sequence decoding.

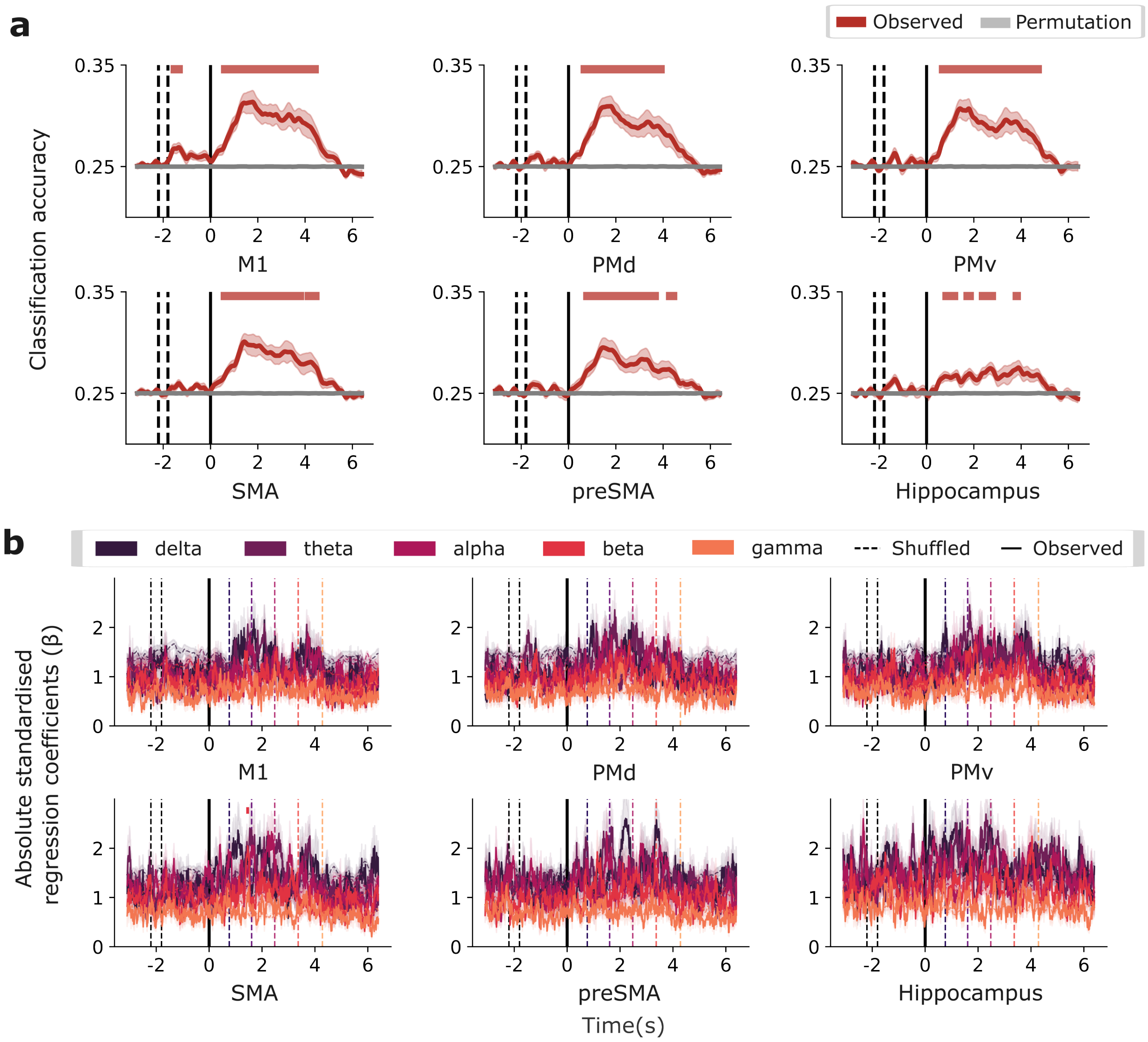

Figure 5: **Sliding window decoding of sequence identity. (a)** Sliding window LDA decoding of sequence identity. A linear discriminant classifier was trained and tested within each time window (200 ms window, 10 ms step) to decode the four finger sequences. Red lines indicate subject averaged classification accuracy based on real labels; gray lines represent chance-level performance(n = 14). Shaded red regions highlight time intervals where decoding exceeded shuffled baseline (cluster forming alpha = .01, final cluster alpha = .05). All motor areas showed above-chance decoding during execution, with region-specific timing differences. The hippocampus exhibited lower decoding accuracy. **(b)** Regression coefficients relating frequency band power to decoder output. Colored lines represent the standardised correlation coefficient of delta (1–4 Hz), theta (4–8 Hz), alpha (8–13 Hz), beta (13–30 Hz), and gamma (30–80 Hz) bands. Colored shading at the top indicates time points with significant correlation relative to the shuffled regression null distribution (cluster forming alpha = .01, final cluster alpha = .05, Bonferroni-corrected across frequency bands).

3. Discussion

Invasive neural recordings in humans and non-human primates reveal a consistent computational principle during the peri-movement phase: cortical motor areas maintain orthogonal population dynamics to functionally separate motor preparation from motor execution, preventing premature motor output [2–4, 29, 30]. Our MEG results in humans extend this notion beyond primarily motor regions in the context of the preparation and execution of movement sequences. We show that the neural activity underlying motor sequence preparation and execution from memory undergoes a pronounced global state shift prior to movement onset across motor, premotor, medial prefrontal and hippocampal regions previously shown to be involved in memory-guided motor sequence control [8, 9]. This fundamental geometric property of neural dynamics ensures the decoupling of planning and acting, whether the motor output is a discrete single action or part of a complex, memory-retrieved behavioural sequence.

Hierarchical transition to execution patterns

Across all regions of interest, the termination of preparatory patterns occurred largely synchronously after the Go Cue, suggesting a global, externally driven reset - here by a visual Go Cue stimulus - propagating to multiple nodes in the network. In contrast, execution-related sequence patterns did not unfold simultaneously. Instead, their onset varied systematically across regions, consistent with a hierarchical organisation and the regions' proximity to the periphery (M1 and motor units in the spinal chord) [28]. In the hippocampus, pre-SMA, and SMA, the shift towards execution patterns appeared $\sim$600 ms or more and $\sim$400 ms before the first button press, whereas in M1, an area closer to the periphery due to dense cortico-spinal outputs, the shift emerged only $\sim$100 ms before finger press onset. Although this temporal ordering aligns with a top–down progression from higher- to lower-level motor-related areas close to the periphery, the $\sim$500 ms delay between the state changes in pre-SMA and M1 cannot be explained by direct cortico-cortical interactions. This points towards an iterative involvement of subcortical, likely striato-thalamo-cortical loops in triggering state-changes across brain regions [31].

Despite evidence for hierarchically timed transitions to execution states, we observed substantial inter-individual variability in the timing of these transitions, particularly in premotor areas and the hippocampus, with some participants showing state transitions to execution driven patterns even before the Go Cue onset. This could reflect differences in task strategy, such as different offsets of abstract sequential cognitive planning versus onsets of lower-level kinaesthetic motor imagery when motor sequences are retrieved from memory and prepared for execution, albeit in the absence of movement.

Across primary motor and premotor cortices, the oscillatory signatures underlying this state transition were not confined to a single frequency band modulation observed during motor preparation and production, such as beta or alpha, but were instead broadband. In contrast, the hippocampus exhibited a band-specific profile, relying primarily on theta activity to predict the transition. Motor state transitions from preparation to execution recruit multiple physiological processes, such as the release of inhibition reflected in beta activity, increases in excitability indexed by alpha (mu) desynchronisation over motor areas [13, 32], and local processing often associated with higher-frequency activity resulting in broadband spectral changes [33]. The hippocampus, in contrast, supports sequence retrieval, and memory-guided planning, functions tightly coupled to theta oscillations. Theta organises hippocampal firing sequences (phase precession, theta sequences) [34] and is the dominant rhythm for these computations. In contrast, hippocampal state transitions are predominantly mediated by theta-dependent phase coding, which is sufficient to represent shifts between mnemonic or planning states [35].

Sequence representations are phase-dependent and dynamic

Whilst the neurophysiological patterns associated with sequence preparation and execution occupied distinct subspaces, suggesting limited overlap in sequence tuning, they were not completely orthogonal and showed significant covariance. This residual overlap suggests that preparing an entire movement sequence inherently recruits components of the execution-related representation. Notably, this stands in contrast to prior findings in single-movement tasks, where preparatory and execution states have been shown to be more cleanly dissociable [3]. One possibility is that motor sequence preparation engages processes akin to motor imagery, whereby aspects of the upcoming movements are internally simulated before execution. Such internal simulation — particularly in the form of kinaesthetic motor imagery [36] — could account for the partial overlap observed between preparatory and execution-related neural states. This overlap may be related to the lack of sequential movement fusion, as the presses, although well-trained were not retrieved as one holistic movement, but as a concatenation of kinematically discrete elements [37, 38].

Neural patterns related the trial phase before and after movement onset accounted for the largest portion of variance in MEG dynamics (dPCA), whereas time and sequence identity had a smaller influence. Notably, whole-sequence patterns did not generalise across the perimovement phase, indicating that sequence-specific coding changes dynamically between motor sequence preparation and execution. In other words, activity does not occur in a separate “space” for each sequence and evolves collectively before and after movement onset, yet each sequence retains its own distinctive trajectory within those subspaces. The most pronounced distance between sequences unfolds in the execution phase when movements diverge in their identity and timing after the first press for execution. The trajectories exhibited regional differences in continuity with more smoothness in M1 versus upstream motor regions. This echoes invasively recorded population pattern trajectories recorded in the context of sequential motor control in non-human primate M1 versus SMA [29].

Although the sequential code was subtle and highly dynamic, MEG patterns still allowed reliable decoding of the press sequences during execution across all motor areas and even before movement onset in M1. While decoding accuracy was modest and far from sufficient for non-invasive BCI applications, it is nevertheless striking that sequential information can be extracted from non-invasive MEG dynamics, given how similar the finger press sequences were: they involved the same digits, half involving the same digit order paired with the different temporal structure, the same number of presses and an identical first digit across sequences within each sequence set per participant. Unlike previous single-cell and fMRI studies reporting premotor tuning to full movement sequences during preparation [8, 20, 39, 40], we found above-chance decoding during preparation confined to M1, with widespread decoding only during execution — a discrepancy that could be resolved via cross-modal fusion analyses [41].

Although decoding accuracy in both preparation and production was found to be related to power changes across multiple oscillatory frequencies, these frequency power modulations explained only up to three percent of the decoding accuracy, suggesting that sequence content is not driven by simple global markers in neuronal excitation and inhibition, such as beta event-related desynchronisation or rebound, e.g. in motor areas.This suggests power alone is not the main driver of decoding; instead, richer phase dynamics encode sequence information.

Recovering motor dynamics from non-invasive brain activity

How can this state shift be picked up with non-invasive recordings such as MEG? While both MEG and invasive electrode arrays offer high temporal resolution, they differ in the types of signals they capture. MEG records extracellular magnetic fields generated by synchronised neuronal currents across large populations of pyramidal neurones [42], whereas microelectrode arrays primarily detect the spiking activity of individual neurones near the electrodes. MEG signals diminish with distance from the source and are especially sensitive to superficial cortical activity [43], whereas invasive electrodes can access deeper layers and brain regions. MEG thus reflects population-level brain oscillations and pre-synaptic neural processing in a brain area. Despite these differences, the overall population-level dynamics successfully capture neural dynamics the major state transitions between movement preparation and execution. This suggests that aspects of internal neural dynamics can be inferred through non-invasive population-level measurements, even in the presence of reduced spatial precision. Non-invasive recordings such as MEG — and, moving forward, OPM-MEG [44] — combined with source reconstruction of individual brain regions, can simultaneously capture activity across multiple areas. This capability is increasingly recognised as critical for BCI development, as focusing solely on M1 overlooks the contributions of a broader network of regions. Accessing signals from multiple areas could provide additional information to improve BCIs' ability to interpret the user's intent [39, 45, 46].

Conclusions

In sum, we show that motor sequence preparation and execution involve a global state shift across motor, premotor and hippocampal regions, unfolding hierarchically between areas removed from the periphery to those with dense cortico-spinal connections. Preparatory and execution-related patterns are largely distinct but partially overlapping, consistent with internal simulation or motor imagery of upcoming sequences. Sequence-specific information is subtle, dynamic, and distributed across multiple frequencies and phases, emerging most strongly during execution but detectable even before movement onset. Critically, non-invasive MEG captures these population-level dynamics, highlighting both fundamental principles of hierarchical motor control and their relevance for brain–computer interfaces, where monitoring multiple regions beyond M1 could enhance decoding of user intent.

4. Methods

4.1. Memory-guided finger sequence task

This study reanalysed MEG data from Kornysheva et al. (2019) [25]. Of the original 16 healthy right-handed participants, 14 were included in the analysis: one was excluded due to motion artefacts, another due to imbalance in sequence accuracy across finger sequences. Participants were trained over two days to associate four abstract visual cues with four five-finger tapping sequences, drawn from a pool of 16 fractal images. Each sequence combined one of two finger orders (F1, F2) with one of two temporal interval orders (T1, T2; 550, 650, 800, 983, and 1300 ms), yielding a 2 × 2 factorial design. For each participant, the identity of the first finger press remained constant across all four sequences. On the third day, participants viewed a visual sequence cue followed by a variable delay (1.8, 2.0, or 2.2 s) and then initiated the memorised sequence upon the Go Cue. Each sequence was presented in groups of three consecutive repetitions, with the order of the groups randomised across the session, for a total of 60 repetitions per sequence. MEG data were continuously recorded at 1200 Hz using a 275-channel axial gradiometer system (CTF Omega, VSM MedTech) in a magnetically shielded room. As in the original study, sensor-level data were preprocessed using Independent Component Analysis (ICA) to remove artefacts and downsampled to 1000 Hz. Trial segments spanned from –2.8 s before to 12 s after sequence cue onset. Only correctly performed trials were included in the analysis, defined by the accurate finger press order and timing within the specified interval windows.

4.2. Statistics analysis

Statistical analyses were performed using non-parametric methods. Group-level omnibus effects were assessed using the Friedman test. Pairwise comparisons were conducted using Wilcoxon signed-rank tests. One-sample comparisons against reference values were performed using one-sample Wilcoxon signed-rank tests. The family-wise error rate was controlled using the Bonferroni correction for fewer than 10 comparisons, and the false discovery rate Benjamini–Hochberg (FDR-BH) procedure for ten or more comparisons. Time-resolved statistics were evaluated using cluster-based permutation testing with a cluster-forming threshold of $p < .01$, and clusters were deemed significant at $p < .05$ with false discovery rate correction.

4.3. MEG source reconstruction

Sensor data were co-registered to a template MRI using fiducial-based alignment in FieldTrip (`http://www.fieldtriptoolbox.org/`, v20241025), based on the nasion and left/right preauricular points. A single-shell volume conduction model was used to compute the leadfield matrix, with grid points defined at 1 cm resolution. Source reconstruction was performed with a linearly constrained minimum variance (LCMV) beamformer. Sensor data were baseline-demeaned using the 1 s interval preceding the sequence cue. A common spatial filter was computed per subject using the whole-trial (14s) covariance matrix, averaged across all correct trials to ensure consistent source orientation.

Motor regions (M1, SMA, pre-SMA, PMd, PMv) were defined using the atlas [47], and the hippocampus using NeuroVault masks [48]. Grid points belonging to each ROI were identified by anatomical labels and aggregated by region. Source time series were extracted at full temporal resolution (1000 Hz). The source channels were sorted and filtered using the anatomical coordinates to ensure consistent and comparable source channels across subjects.

4.4. Time frequency analysis and cluster-based statistical testing

Time–frequency representations (TFRs) were computed from the source-localised data (1000Hz) using the multitaper method. Data were aligned to the Go Cue without truncation and mirror-padded to 40 s to prevent edge artefacts. Spectrum power was estimated from 0.5 to 80 Hz in 0.5 Hz step and 50 ms timestep. Hanning taper with a window length of six cycles per frequency were applied.

For visualisation, TFRs were dB-normalised relative to 1 s baseline period prior to Go Cue individually and then grand-averaged across participants. Group-level baseline demeaning was performed to centre baseline grand-average activity to zero.

Statistical evaluation of task-related power changes was performed using a cluster-based permutation test (FieldTrip function `ft_freqstatistics`). The 1 s baseline period was repeated to match the task window length. Significance was assessed using a Monte Carlo method with dependent-samples t-statistics (cfg.method = `'montecarlo'`, cfg.statistic = `'depsamplesT'`, cfg.correctm = `'cluster'`). The cluster-forming threshold was set at clusteralpha = .01, and post-permutation clusters were considered significant at alpha = .05.

4.5. Linear discriminant analysis on phase prediction

Linear Discriminant Analysis (LDA) was applied to source-reconstructed time series, downsampled to 200 Hz. For each participant, the classifier was trained to discriminate between eight conditions defined by a 2×4 factorial design: task phase (preparation vs execution) crossed with sequence identity (sequences 1–4). This yielded the following labels: prep×seq1, exec×seq1, ..., prep×seq4, exec×seq4. The preparation period was defined from sequence cue onset to the variable Go Cue; execution spanned from the first to the final finger press, defined based on trial-wise variable timing.

Decoding results were averaged across 1,000 bootstraps. For each iteration, 40 correctly performed trials were sampled per sequence (or the maximum number of available trials if fewer; only participant had fewer trials than 40 trials for one sequence) and split into training and test sets ($70/30$ ratio), with stratification to maintain sequence balance. Samples equivalent of 1 s length was randomly extracted from either the preparation or execution period of each training trial and labelled by phase–sequence identity. The trained classifier was then applied continuously to the full test-trial time course to obtain decoding probability trajectories.

Chance level baselines were generated by repeating this procedure with randomly permuted class labels while controlling all other processing steps constant. Classification accuracy values represent the time-resolved accuracy of assigning the correct phase–sequence label, calculated exclusively from test trials of the matching sequence. For visualisation, accuracy curves were first averaged across repeats within participants, then aggregated mean and standard error (SEM) across participants. The cluster-based permutation test performed across observed and permuted decoding curves (clusteralpha = .01, final cluster alpha = .05, Bonferroni-correction over 2 phases).

To quantify the timing of phase transitions, decoding curves were aligned to task events to account for the variable Go Cue and press timing. Go Cue aligned prediction curves were used to measure the offset of preparation patterns and first press alignment for the onset of execution patterns. Cluster-based permutation significance is computed per participant using the 1,000 bootstraps of observed trials and permutation probability (clusteralpha = .01, final cluster alpha = .05, Bonferroni-correction over 2 phases). Significant clusters shorter than 10 ms were discarded, and clusters separated by less than 10 ms were merged before extracting timing estimates.

4.5.1. Linear mixed-effects models testing hierarchical trend in transition timings

To test whether the timing of neural state transitions followed the assumed cortical–hippocampal hierarchy, we defined the ordinal rank of regions with the reported anatomical density of direct cortico-spinal projections to the lower cervical segments of the spinal cord (C7–T1) and cortico-cortical connectivity to M1: Hippocampus (Rank = 1), pre-SMA(Rank = 2), SMA(Rank = 3), PMv(Rank = 4), PMd(Rank = 5) and M1(Rank = 6).

For each transition type, we fitted a linear mixed-effects model of the form:

$$\text{Transition Time}_{ij} = \beta_0 + \beta_1\,\text{Rank}_{ij} + u_{0j} + \varepsilon_{ij},$$

where β_0 is the intercept, β_1 indexes the linear trend across the hierarchical axis, u_{0j} is a random intercept for subject j, and ε_{ij} is residual error.

A negative β_1 indicates progressively earlier transitions toward M1 (hippocampus $\rightarrow$ M1), whereas a positive β_1 reflects the opposite trend. Standardised coefficients were computed to provide an interpretable effect size:

$$\beta_1^* = \beta_1 \times \left(\frac{\mathrm{SD}(\text{Rank})}{\mathrm{SD}(\text{Transition Time})} \right),$$

representing the change in onset time (in SD units) per SD change in region rank.

Two-tailed tests were performed for β_1 ($H_0 : \beta_1 = 0$), with significance defined as $\alpha = 0.05$.

4.6. Regression of canonical frequency power onto LDA-derived state estimates

To relate frequency-specific neural activity to the emergence of preparation and execution patterns, LDA predictions were regressed against canonical frequency band power. Time–frequency representations (TFRs) were computed for each participant using the same setting as above, but at high temporal resolution (200 Hz) to match both the sampling rate and temporal structure of the LDA output. Spectral power was extracted for five canonical frequency bands: delta ($1 - 4Hz$), theta ($4 - 8Hz$), alpha ($8 - 13Hz$), beta ($13 - 30Hz$), and gamma ($30 - 80Hz$). TFRs were z-scored per trial and then averaged across trials within each sequence and frequency band.

To examine the relationship between spectral dynamics and execution-related decoding, LDA predictions were z-scored then averaged across 1,000 bootstrap repeats per sequence. Time-resolved correlations were computed using a sliding window approach at 200 ms window and 10 ms step. For each window, a predictor matrix $X \in \mathbb{R}^{160\times 5}$ (4 sequences × 40 timepoints × 5 bands) was regressed against the corresponding LDA predictions $y \in \mathbb{R}^{160}$ (4 sequences × 40 timepoints) using ridge regression with a regularisation parameter of $\alpha = 1$.

Statistical significance was assessed using the cluster based permutation test against the permuted correlation curve (cluster-forming alpha = .05; corrected alpha = .01, Bonferroni-corrected over 5 frequencies). The permutation correlation curve was generated by circularly shifting the predictor time series with a minimum shift of 10% of the trial time length across 1000 repeats.

A similar analysis was performed to assess the relationship between spectral dynamics and sequence identity predictions. In this case, the LDA classifier already yielded time-resolved sequence predictions using the same sliding-window configuration (200 ms window, 10 ms step). The spectral predictors were temporally aligned to the corresponding LDA output for each window. The predictors were z-scored along the time dimension, and ridge regression ($\alpha = 1$) was applied at each time window. Statistical assessment followed the same permutation framework as described above. For each participant, a null distribution of regression coefficients was generated by 1000 repeats of circularly shifting the LDA prediction time windows.

4.7. Principal component analysis

Principal component analysis (PCA) was performed separately for each participant using source-reconstructed data binned at 200 Hz. The dimensionality of the data was reduced to the first 10 principal components (PCs), or to the minimum number of available source channels if fewer than 10. For visualisation, PCA-transformed time series were averaged across trials for each sequence condition and smoothed using a one-dimensional Gaussian filter ($\sigma = 25$ ms).

4.7.1. Kolmogorov–Smirnov distance

To quantify separation between preparation and execution activity along each principal component, the Kolmogorov–Smirnov (KS) distance was computed between their respective distributions. To account for unequal sample sizes, 1 000 bootstrap iterations were performed in which 500 time points were randomly drawn from each phase. The null distribution was constructed by repeating the same procedural with randomly permuted phase labels. KS distances were averaged across bootstrap repetitions for each participant, and group-level differences between observed and null values were assessed using paired Wilcoxon signed-rank tests, FDR-BH over 3 PCs x 6 areas.

Separation between preparatory and execution states was quantified as the mean Euclidean distance between execution-phase points and the preparatory centroid:

$$D_{exec\to prep} = \frac{1}{n}\sum_{i=1}^{n}\left\|\mathbf{x}_i - \boldsymbol{\mu}_{prep}\right\|_2, \quad \text{where} \quad \boldsymbol{\mu}_{prep} = \frac{1}{m}\sum_{j=1}^{m}\mathbf{y}_j$$

Distance per participant were obtained using bootstrap resampling (1,000 iterations; 500 samples per phase) with an identical phase-shuffled permutation procedure to generate a null distribution. Group-level effects were assessed using paired Wilcoxon signed-rank tests with FDR correction.

4.7.2. Alignment index

To assess the alignment of subspaces between preparatory and execution dynamics [49], separate principal component analyses (PCA) were performed on data corresponding to the preparation (prepPCA) and execution phases(execPCA).

$$\text{Alignment} = \frac{1}{k}\operatorname{Tr}\left(U_{\text{exec}}^{\top} P_{\text{prep}} U_{\text{exec}}\right) = \frac{1}{k}\operatorname{Tr}\left(U_{\text{exec}}^{\top} U_{\text{prep}} U_{\text{prep}}^{\top} U_{\text{exec}}\right).$$

where U_{prep} and U_{exec} are the PCA basis matrices (with orthonormal columns) for the preparatory and execution subspaces, respectively, and $P_{\text{prep}} = U_{\text{prep}} U_{\text{prep}}^{\top}$ is the projection operator onto the preparatory subspace. The alignment index measures the extent to which the execution components lie within the preparatory subspace. A value of 1 indicates perfect alignment, while lower values indicate greater orthogonality. Statistical significance was assessed by comparing the alignment index against 1 using a one-sample Wilcoxon signed-rank tests

4.7.3. Gaussian mixture model and rotation angle

The angle between preparatory and execution states was quantified in low-dimensional PCA space. For each participant and each brain region, a one-component Gaussian mixture model was fitted separately to preparation and execution distributions derived from the first three PCs of the sequence-averaged embeddings. The principal direction of each state was defined as the eigenvector associated with the largest eigenvalue of the fitted covariance matrix. Eigenvectors were sign-aligned by enforcing a positive first component to ensure directional consistency across states and subjects.

Angles between states were computed using the dot-product–based acute angle measure:

$$\theta = \arccos\left(|\mathbf{v}_{prep} \cdot \mathbf{v}_{exec}|\right)$$

yielding distances constrained to the range $0^\circ - 90^\circ$. For each region, one-sample Wilcoxon signed-rank tests were used to assess whether preparation - execution angles differed from no rotation (0°) and orthogonality (90°) (Bonferroni correction over 6 areas).

4.8. Covariance matrix and t-distributed stochastic neighbour

To visualise temporal changes in covariance structure, we performed a sliding-window covariance analysis on data downsampled to 200 Hz, using a 200 ms window and a 10 ms step. For each participant, covariance matrices were computed across trials and averaged within each sequence without further preprocessing. The resulting covariance matrices were then vectorised and embedded into a low-dimensional space using t-distributed stochastic neighbour embedding (t-SNE) (perplexity=5, ndim = 3).

Two summary measures were derived from the embedded covariance trajectories. The mean consecutive euclidean distance was computed by taking the Euclidean distance between successive sequence-averaged embeddings in the 3-dimensional space. The euclidean distance between preparation and execution phases was quantified using a bootstrap (1000 repeats): in each iteration, an equal number of samples per phase (N = 500) was drawn, and the Euclidean distance between the execution-state points and the centroid of the preparation-state points was calculated.

4.8.1. Correlation distance between phases

To quantify similarity in covariance structure between preparatory and execution periods, trial-wise covariance matrices were first labelled and grouped according to phase identity. Similarity was estimated using a bootstrap procedure applied separately for each participant. In each iteration, 10,000 bootstrap samples were drawn from each phase and averaged, and covariance similarity was quantified using correlation distance:

$$d = 1 - \text{corr}\left(\text{vec}(C_{\text{prep}}), \text{vec}(C_{\text{exec}})\right),$$

where C_{prep} and C_{exec} denote the averaged covariance matrices for the preparatory and execution states, respectively, and $\text{vec}(\cdot)$ refers to vectorisation of the upper triangular matrix excluding the diagonal. A null distribution was generated by repeating the full procedure after randomly permuting phase labels, thereby removing the systematic preparatory–execution structure while preserving covariance magnitude and sampling statistics.

4.9. Demixed PCA

Demixed principal component analysis (dPCA) was applied to separate sources of variance attributable to time, sequence identity, and their interaction within the 200 Hz source-reconstructed time series [50]. For each participant and each brain region, dPCA was performed on correct trials, using the minimum number of correct trials available across sequences to ensure balanced input. The dPCA input had dimensionality $\mathrm{n}_{\mathrm{sequence}} \times \mathrm{n}_{\mathrm{repeats}} \times \mathrm{n}_{\mathrm{time}}$, and the decomposition yielded three sets of principal components corresponding to the *time*, *sequence*, and *time*$\sim\times\sim$*sequence* marginalizations. For each marginalisation, explained variance was quantified and the variance of the top three components was summed. To quantify separability between sequences in the source × time component space, a sliding-window analysis (200 ms window, 10 ms step) was applied to compute pairwise Euclidean distances between sequence centroids at each time point. The resulting distances were then averaged across all pairwise comparisons to yield a summary measure of sequence separation.

4.10. Sliding window LDA for sequence decoding

Sliding-window linear discriminant analysis (LDA) was performed using a 200 ms window with a 10 ms step size on the 200 Hz source-level time series. For each subject, 40 correct trials per sequence were randomly sampled without replacement, and data were split into training and test sets using a 70/30 stratified split. Within each time window, the LDA classifier was trained on the corresponding training-set segment and evaluated on the matching held-out test segment. Decoding accuracy was computed as the proportion of correctly classified test-set samples and then averaged across all time points within the window.

This sampling and decoding procedure was repeated 500 times per participants to estimate robust average decoding performance. Final accuracy time courses were obtained by averaging across repetitions. No temporal smoothing was applied. All analyses were performed independently for each brain region.

Statistical significance was assessed using a cluster-based permutation test relative to the permuted baseline (cluster forming threshold = .01, cluster-level significance = .05). For each participant, a null distribution was generated by repeating the decoding procedure with randomly permuted sequence labels (500 permutations). Observed decoding accuracy was then compared against this null distribution to determine whether performance exceeded chance.

4.11. Ethical Statement

In the original study [25], all participants gave written informed consent to participate. The study was approved by the University College London Research Ethics Committee for Human-Based Research (UCL Ethics ID: 1338/006, Data Protection: Z6364106/2011/10/25). All participants were financially compensated for their participation.

Acknowledgments

This work was supported by a UKRI Future Leaders Fellowship awarded to K.K. (MR/Y016467/1). This work was partially supported by BlueBEAR and Baskerville, funded by the EPSRC and UKRI through the World Class Labs scheme (EP/T022221/1) and the Digital Research Infrastructure programme (EP/W032244/1) and operated by Advanced Research Computing at the University of Birmingham.

References

[1] Mark M Churchland. When preparation pays off. *ELife*, 13:e102187, 2024.

[2] Mark M. Churchland, John P. Cunningham, Matthew T. Kaufman, Justin D. Foster, Paul Nuyujukian, Stephen I. Ryu, and Krishna V. Shenoy. Neural population dynamics during reaching. *Nature*, 487(7405):51–56, 2012. doi: 10.1038/nature11129.

[3] Matthew T Kaufman, Mark M Churchland, Stephen I Ryu, and Krishna V Shenoy. Cortical activity in the null space: permitting preparation without movement. *Nature neuroscience*, 17(3): 440–448, 2014.

[4] Gamal F. Elsayed, Ariel H. Lara, Matthew T. Kaufman, Mark M. Churchland, and John P. Cunningham. Reorganization between preparatory and movement population responses in motor cortex. *Nature Communications*, 7:13239, 2016. doi: 10.1038/ncomms13239.

[5] Mark M. Churchland and Krishna V. Shenoy. Preparatory activity and the expansive null-space. *Nature Reviews Neuroscience*, 25(4):213–236, April 2024. ISSN 1471-0048. doi: 10.1038/s41583-024-00796-z. Publisher: Nature Publishing Group.

[6] Ta-Chu Kao, Mahdieh S Sadabadi, and Guillaume Hennequin. Optimal anticipatory control as a theory of motor preparation: A thalamo-cortical circuit model. *Neuron*, 109(9):1567–1581, 2021.

[7] Krishna V Shenoy, Maneesh Sahani, and Mark M Churchland. Cortical control of arm movements: a dynamical systems perspective. *Annual review of neuroscience*, 36(1):337–359, 2013.

[8] Rhys Yewbrey, Myrto Mantziara, and Katja Kornysheva. Cortical patterns shift from sequence feature separation during planning to integration during motor execution. *Journal of Neuroscience*, 43(10):1742–1756, 2023.

[9] Rhys Yewbrey and Katja Kornysheva. The hippocampus preorders movements for skilled action sequences. *Journal of Neuroscience*, 44(45), 2024.

[10] Michael T Jurkiewicz, William C Gaetz, Andreea C Bostan, and Douglas Cheyne. Post-movement beta rebound is generated in motor cortex: evidence from neuromagnetic recordings. *Neuroimage*, 32(3):1281–1289, 2006.

[11] Andreas K Engel and Pascal Fries. Beta-band oscillations—signalling the status quo? *Current opinion in neurobiology*, 20(2):156–165, 2010.

[12] Suresh D Muthukumaraswamy, Blake W Johnson, and Nicolas A McNair. Mu rhythm modulation during observation of an object-directed grasp. *Cognitive brain research*, 19(2):195–201, 2004.

[13] Jacopo Barone and Holly E Rossiter. Understanding the role of sensorimotor beta oscillations. *Frontiers in systems neuroscience*, 15:655886, 2021.

[14] Rosamund Hannah, Sarah E. Cavanagh, Sébastien Tremblay, Sonia Simeoni, and John C. Rothwell. Selective suppression of local interneuron circuits in human motor cortex contributes to movement preparation. *Journal of Neuroscience*, 38(5):1264–1276, 2018. doi: 10.1523/JNEUROSCI.2869-17.2017.

[15] Debadatta Dash, Fumiaki Iwane, William Hayward, Roberto Salamanca-Giron, Marlene Bonstrup, Ethan R Buch, and Leonardo G Cohen. Sequence action representations contextualize during early skill learning. *bioRxiv*, pages 2024–08, 2024.

[16] Atsushi Kikumoto and Ulrich Mayr. Decoding hierarchical control of sequential behavior in oscillatory eeg activity. *Elife*, 7:e38550, 2018.

[17] Andrew J Zimnik and Mark M Churchland. Independent generation of sequence elements by motor cortex. *Nature neuroscience*, 24(3):412–424, 2021.

[18] Giacomo Ariani, J. Andrew Pruszynski, and Jørn Diedrichsen. Motor planning brings human primary somatosensory cortex into action-specific preparatory states. *eLife*, 11:e69517, 2022. doi: 10.7554/eLife.69517.

[19] Brian M Dekleva, Konrad P Kording, and Lee E Miller. Single reach plans in dorsal premotor cortex during a two-target task. *Nature communications*, 9(1):3556, 2018.

[20] Keisetsu Shima and Jun Tanji. Neuronal activity in the supplementary and presupplementary motor areas for temporal organization of multiple movements. *Journal of neurophysiology*, 84 (4):2148–2160, 2000.

[21] Atsushi Yokoi and Jørn Diedrichsen. Neural organization of hierarchical motor sequence representations in the human neocortex. *Neuron*, 103(6):1178–1190, 2019.

[22] Nina Dolfen, Serena Reverberi, Hans Op de Beeck, Bradley R King, and Genevieve Albouy. The hippocampus represents information about movements in their temporal position in a learned motor sequence. *Journal of Neuroscience*, 44(37), 2024.

[23] Serena Reverberi, Nina Dolfen, Bradley Ross King, and Genevieve Albouy. Motor cortical areas facilitate schema-mediated integration of new motor information into memory. *bioRxiv*, pages 2025–08, 2025.

[24] Ethan R Buch, Leonardo Claudino, Romain Quentin, Marlene Bönstrup, and Leonardo G Cohen. Consolidation of human skill linked to waking hippocampo-neocortical replay. *Cell reports*, 35 (10), 2021.

[25] Katja Kornysheva, Daniel Bush, Sofie S Meyer, Anna Sadnicka, Gareth Barnes, and Neil Burgess. Neural competitive queuing of ordinal structure underlies skilled sequential action. *Neuron*, 101(6):1166–1180, 2019.

[26] Nora A Herweg, Ethan A Solomon, and Michael J Kahana. Theta oscillations in human memory. *Trends in cognitive sciences*, 24(3):208–227, 2020.

[27] Tuba Aktürk, Tom A de Graaf, Furkan Erdal, Alexander T Sack, and Bahar Güntekin. Oscillatory delta and theta frequencies differentially support multiple items encoding to optimize memory performance during the digit span task. *NeuroImage*, 263:119650, 2022.

[28] Richard P Dum and Peter L Strick. Frontal lobe inputs to the digit representations of the motor areas on the lateral surface of the hemisphere. *Journal of Neuroscience*, 25(6):1375–1386, 2005.

[29] Abigail A Russo, Ramin Khajeh, Sean R Bittner, Sean M Perkins, John P Cunningham, Laurence F Abbott, and Mark M Churchland. Neural trajectories in the supplementary motor area and motor cortex exhibit distinct geometries, compatible with different classes of computation. *Neuron*, 107(4):745–758, 2020.

[30] Brian M Dekleva, Raeed H Chowdhury, Aaron P Batista, Steven M Chase, Byron M Yu, Michael L Boninger, and Jennifer L Collinger. Motor cortex retains and reorients neural dynamics during motor imagery. *Nature human behaviour*, 8(4):729–742, 2024.

[31] Laureline Logiaco, LF Abbott, and Sean Escola. Thalamic control of cortical dynamics in a model of flexible motor sequencing. *Cell reports*, 35(9), 2021.

[32] Bernadette CM van Wijk, Peter J Beek, and Andreas Daffertshofer. Neural synchrony within the motor system: what have we learned so far? *Frontiers in human neuroscience*, 6:252, 2012.

[33] Pascal Fries. Neuronal gamma-band synchronization as a fundamental process in cortical computation. *Annual review of neuroscience*, 32(1):209–224, 2009.

[34] György Buzsáki and Edvard I Moser. Memory, navigation and theta rhythm in the hippocampal-entorhinal system. *Nature neuroscience*, 16(2):130–138, 2013.

[35] H Freyja Ólafsdóttir, Daniel Bush, and Caswell Barry. The role of hippocampal replay in memory and planning. *Current Biology*, 28(1):R37–R50, 2018.

[36] Cathy M Stinear, Winston D Byblow, Maarten Steyvers, Oron Levin, and Stephan P Swinnen. Kinesthetic, but not visual, motor imagery modulates corticomotor excitability. *Experimental brain research*, 168(1):157–164, 2006.

[37] Rebecca MC Spencer and Richard B Ivry. Comparison of patients with parkinson's disease or cerebellar lesions in the production of periodic movements involving event-based or emergent timing. *Brain and cognition*, 58(1):84–93, 2005.

[38] Helena Wright-Wieckowski, Jason Friedman, Joseph M Galea, and Katja Kornysheva. Competitive pre-ordering during planning persists in kinematically fused sequential movements. *bioRxiv*, pages 2025–08, 2025.

[39] Jun Tanji and Keisetsu Shima. Role for supplementary motor area cells in planning several movements ahead. *Nature*, 371(6496):413–416, 1994.

[40] Giacomo Ariani, Mahdiyar Shahbazi, and Jörn Diedrichsen. Cortical areas for planning sequences before and during movement. *Journal of Neuroscience*, 45(3), 2025.

[41] Radoslaw M Cichy and Aude Oliva. Am/eeg-fmri fusion primer: resolving human brain responses in space and time. *Neuron*, 107(5):772–781, 2020.

[42] Sylvain Baillet. Magnetoencephalography for brain electrophysiology and imaging. *Nature neuroscience*, 20(3):327–339, 2017.

[43] Arjan Hillebrand and Gareth R Barnes. A quantitative assessment of the sensitivity of whole-head meg to activity in the adult human cortex. *Neuroimage*, 16(3):638–650, 2002.

[44] Elena Boto, Niall Holmes, James Leggett, Gillian Roberts, Vishal Shah, Sofie S Meyer, Leonardo Duque Muñoz, Karen J Mullinger, Tim M Tierney, Sven Bestmann, et al. Moving magnetoencephalography towards real-world applications with a wearable system. *Nature*, 555 (7698):657–661, 2018.

[45] Juan A Gallego, Tamar R Makin, and Samuel D McDougle. Going beyond primary motor cortex to improve brain–computer interfaces. *Trends in neurosciences*, 45(3):176–183, 2022.

[46] Richard A Andersen, Tyson Aflalo, and Spencer Kellis. From thought to action: The brain–machine interface in posterior parietal cortex. *Proceedings of the National Academy of Sciences*, 116(52):26274–26279, 2019.

[47] Mary A Mayka, Daniel M Corcos, Sue E Leurgans, and David E Vaillancourt. Three-dimensional locations and boundaries of motor and premotor cortices as defined by functional brain imaging: a meta-analysis. *Neuroimage*, 31(4):1453–1474, 2006.

[48] Krzysztof J Gorgolewski, Gael Varoquaux, Gabriel Rivera, Yannick Schwarz, Satrajit S Ghosh, Camille Maumet, Vanessa V Sochat, Thomas E Nichols, Russell A Poldrack, Jean-Baptiste Poline, et al. Neurovault. org: a web-based repository for collecting and sharing unthresholded statistical maps of the human brain. *Frontiers in neuroinformatics*, 9:8, 2015.

[49] Katherine Cora Ames and Mark M Churchland. Motor cortex signals for each arm are mixed across hemispheres and neurons yet partitioned within the population response. *Elife*, 8:e46159, 2019.

[50] Dmitry Kobak, Wieland Brendel, Christos Constantinidis, Claudia E Feierstein, Adam Kepecs, Zachary F Mainen, Xue-Lian Qi, Ranulfo Romo, Naoshige Uchida, and Christian K Machens. Demixed principal component analysis of neural population data. *elife*, 5:e10989, 2016.